

ADVANCED MATERIALS

Supporting Information

for *Adv. Mater.*, DOI: 10.1002/adma.201701494

Antipulverization Electrode Based on Low-Carbon Triple-Shelled Superstructures for Lithium-Ion Batteries

Lianhai Zu, Qingmei Su, Feng Zhu, Bingjie Chen, Huanhuan Lu, Chengxin Peng, Ting He, Gaohui Du, Pengfei He, Kai Chen, Shihe Yang, Jinhui Yang, and Huisheng Peng**

Supporting Information

1
2
3
4
5
6
7
8
9
10
11
12
13
14
15
16
17
18
19
20
21
22
23
24
25
26
27
28
29**Experimental Section**

Chemicals and Materials. Tin tetrachloride anhydrous (SnCl_4 , 98%), sodium hydroxide (NaOH), urea (H_2NCONH_2), $\text{NH}_3\cdot\text{H}_2\text{O}$ solution (25%) and tetraethylorthosilicate (TEOS) were purchased from Aladdin Biological Technology Co., Ltd. (China). Sodium dodecyl sulfate (SDS) was purchased from Alfa Aesar Chemical Co., Ltd. (China). Ethanol and glucose were purchased from Sinopharm Chemical Reagent Co., Ltd. (China). Tin dioxide (SnO_2 , 20-50 nm) was purchased from Adamas Reagent Co., Ltd. (China).

Preparation of SiO_2 nanospheres. An aqueous solution was prepared by mixing 3.14 mL of concentrated $\text{NH}_3\cdot\text{H}_2\text{O}$ solution (25%, w/w), 74 mL of ethanol and 10 mL of deionized (DI) water under stirring for 0.5 h. Then, 6 mL of tetraethylorthosilicate (TEOS) was injected, forming an opalescent reacting solution. After reaction for 22 h under stirring at 300 rpm, the SiO_2 nanospheres were formed, collected by centrifugation and washed with ethanol 3 times.

Preparation of SnO_2 double-shelled hollow superstructures (DSHSs). Urea (1.8 g), 0.315 g of $\text{Na}_2\text{SnO}_3\cdot 3\text{H}_2\text{O}$ and 800 mg of glucose ($\text{C}_6\text{H}_{12}\text{O}_6$) were dissolved in 50 mL of DI water, followed by the addition of 27 mL of ethanol under stirring, resulting in a milky suspension. Another suspension was prepared separately by dispersing 240 mg of the SiO_2 nanospheres in 4 mL of water under sonication. The two suspensions were mixed and transferred to a 100 mL Teflon autoclave. The reaction system was placed in an electric oven and kept at 190 °C for 36 h, leading to a gray precipitate. Finally, the product was centrifuged, washed with DI water and dried for further use.

Preparation of SnO_2 triple-shelled hollow superstructures (TSHSs). a) SnO_2 seed loading on the surface of SnO_2 DSHSs. In a typical synthesis, 30 mg of SnO_2 DSHS powders were dispersed in 40 mL of 5 mM SnCl_4 aqueous solution under vigorous stirring. After 12 h, the resulting powders were collected and rinsed several times with distilled water and ethanol.

b) Growth of SnO_2 nanorod arrays on the surfaces of SnO_2 seed-loaded DSHS. A precursor solution containing 5 mM SnCl_4 , 1 M NaOH, and 0.33 M SDS (sodium dodecyl sulfate) was prepared beforehand. Then, 50 mg of SnO_2 seed-loaded DSHSs was injected into the precursor solution with

1 sonication, resulting in a uniform suspension. Then, the suspension was transferred into a Teflon lined
2 autoclave (25 mL) with a stainless-steel shell, and kept at 205 °C in an oven. After reacting for 15 h, a
3 gray precipitate was produced. The product was washed with water and alcohol several times to
4 remove possible residues.

5 c) Deposition of thin layers of graphenized carbon on SnO₂ TSHSs. The SnO₂ TSHS powder (200 mg)
6 in a crucible was positioned into a tube furnace. Then, 20 sccm of gas mixture (10% C₂H₂ and 90%
7 N₂) was introduced for 40 min at 400 °C, resulting in a brown powder. The powder was then annealed
8 at 550 °C under nitrogen atmosphere. After 6 h, the final black powder was obtained.

9 *Electrochemical measurements.* Electrochemical tests were performed using coin-type half-cells (2016
10 size) that were assembled in an argon-filled glove box. The working electrode was made by mixing
11 70% active material (carbon-coated SnO₂ TSHSs), 20% super-p carbon black and 10%
12 poly(vinylidene fluoride) (PVDF) binder on a copper foil. The electrolyte was 1.0 M LiPF₆ with 1:1
13 ethylene carbonate/diethylene carbonate (EC/DMC). The loading mass of the active materials (Ø =14
14 mm) is 3.5 – 4.9 mg (1.8-2.5 mg cm⁻²) for the TSHSs and 1.3-1.8 mg (0.7-0.9 mg cm⁻²) for the DSHSs.
15 Glass fibers (GF/D) from Whatman were used as separators, and pure lithium metal foil was used as
16 the counter electrode. The cycle performance of the cells was tested at different rates within a fixed
17 voltage window of 2.5 V-5 mV vs. Li⁺/Li at room temperature. The rate capability was evaluated by
18 varying the discharge/charge rate from 0.2-16 A g⁻¹. All the capacities were calculated based on the
19 total weight of carbon and tin dioxide.

20 *Characterizations.* The crystal structures and morphologies of the as-synthesized composites were
21 characterized by powder X-ray diffraction (XRD, Bruker D8 Advance , Cu Kα radiation), field-
22 emission scanning electron microscopy (SEM, Hitachi S-4800, 3 and 15kV), transmission electron
23 microscopy (TEM) and high-resolution transmission electron microscope (HRTEM, JEOL JEM2100F,
24 200 kV) together with associated energy-dispersive X-ray spectroscopy (EDS). Nitrogen adsorption–
25 desorption isotherms were recorded on an ASAP 2420 instrument. Before the measurements, the
26 sample was degassed in vacuum at 200 °C for at least 8 h. The Brunauer-Emmett- Teller method was
27 utilized to calculate the surface areas. The pore size distributions were retrieved by using the Barrett-
28 Joyner-Halanda (BJH) method from the adsorption branch of the isotherms. The contents of Carbon

1 element in the DSHSs and TSHSs were measured by a differential thermal analyzer (DTA)
2 (NETZSCH DTA 409 PC).

3 *In situ TEM.*

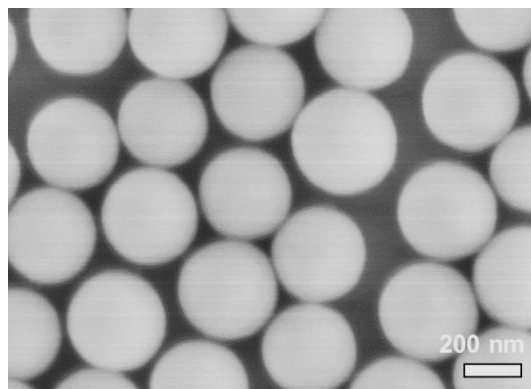
4 *In situ* mechanical tests .The SnO₂ TSHSs were suspended in ethanol by ultrasonic dispersion for
5 half an hour and the TSHSs dispersed in droplets were transferred to a Si wedge, which was specially
6 designed to facilitate the TEM study of micro/nano particulates^{1,2}. The *in situ* mechanical tests on
7 individual TSHSs were conducted under displacement control mode inside a JEOL 2100F TEM which
8 was equipped with a PicoIndenter (Hysitron PI95 ECR) sample holder. The deformation process and
9 morphology evolution of each TSHS under compressive loading was observed and a real time video
10 was taken using a Gatan 833 CCD camera (SC200) at the rate of 10 frame/second, and in the
11 meanwhile the force imposed onto the TSHS was recorded.

12 *In situ electrochemical tests.* The *in situ* nanoscale electrochemical tests were conducted inside a
13 JEM-2100F transmission electron microscope using a Nanofactory TEM-scanning tunneling
14 microscopy (STM) holder. To determine the current–voltage behavior of the samples, TSHSs and
15 DSHSs were separately attached to a 0.25 mm Au wire, serving as the working electrodes. A tungsten
16 (W) STM tip was used to scratch the Li metal surface to obtain fresh Li metal inside a glovebox filled
17 with argon. The surface layer of Li on the tip of the W rod served as the counter electrode and lithium
18 source. Both the SnO₂ and lithium electrodes were mounted onto a Nanofactory STM-TEM holder,
19 which was quickly transferred into the TEM column. A native Li₂O layer formed on the surface of the
20 Li metal due to the exposure to air, which served as the solid-state electrolyte to allow the transport of
21 Li-ions. The Li₂O/Li electrode attached to the mobile STM probe was driven to contact the SnO₂
22 electrode inside the transmission electron microscope. Lithiation occurred after a negative bias (-3 V)
23 was applied to the SnO₂ electrode with respect to the lithium electrode to drive Li⁺ to transport through
24 the solid-state Li₂O layer, and the bias was then reversed to positive (+3 V) to facilitate the process of
25 delithiation in which Li ions were driven through the solid electrolyte.

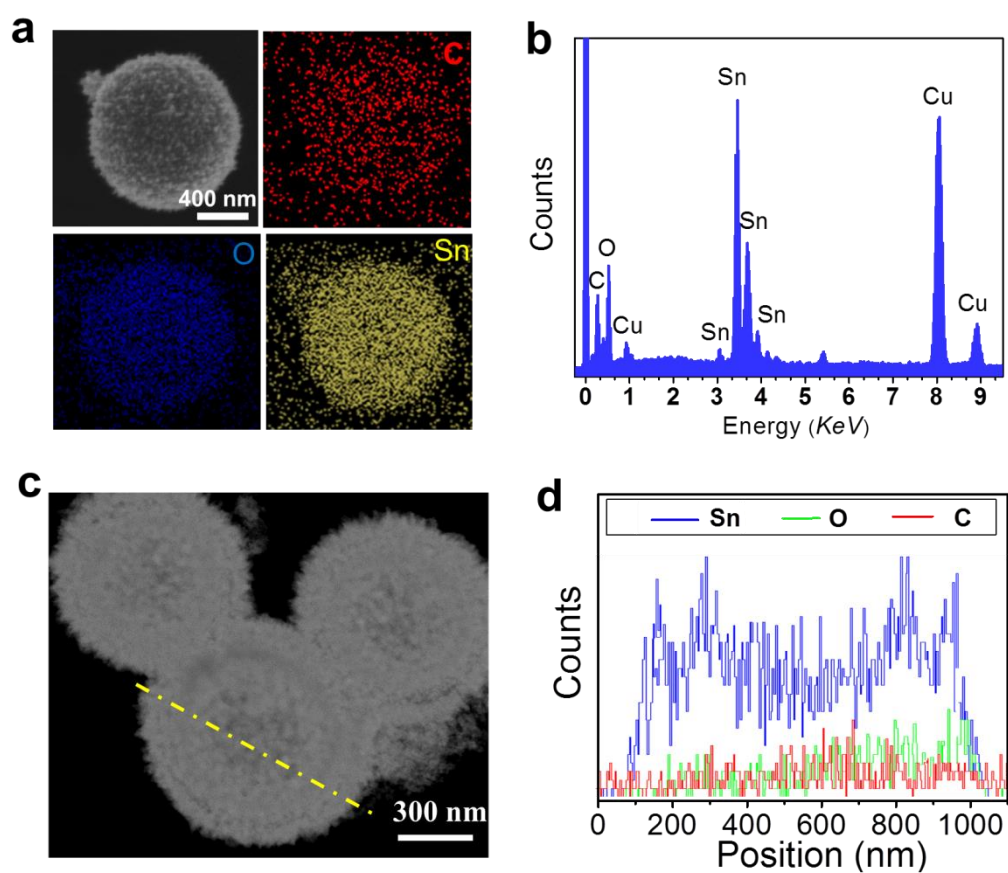
26

27

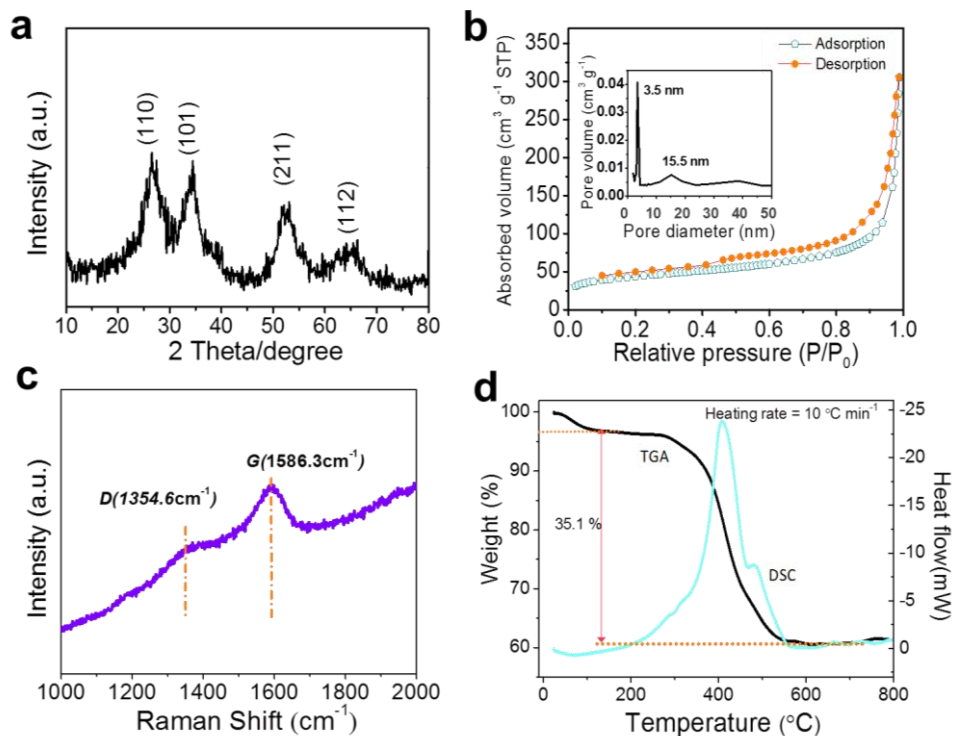
28



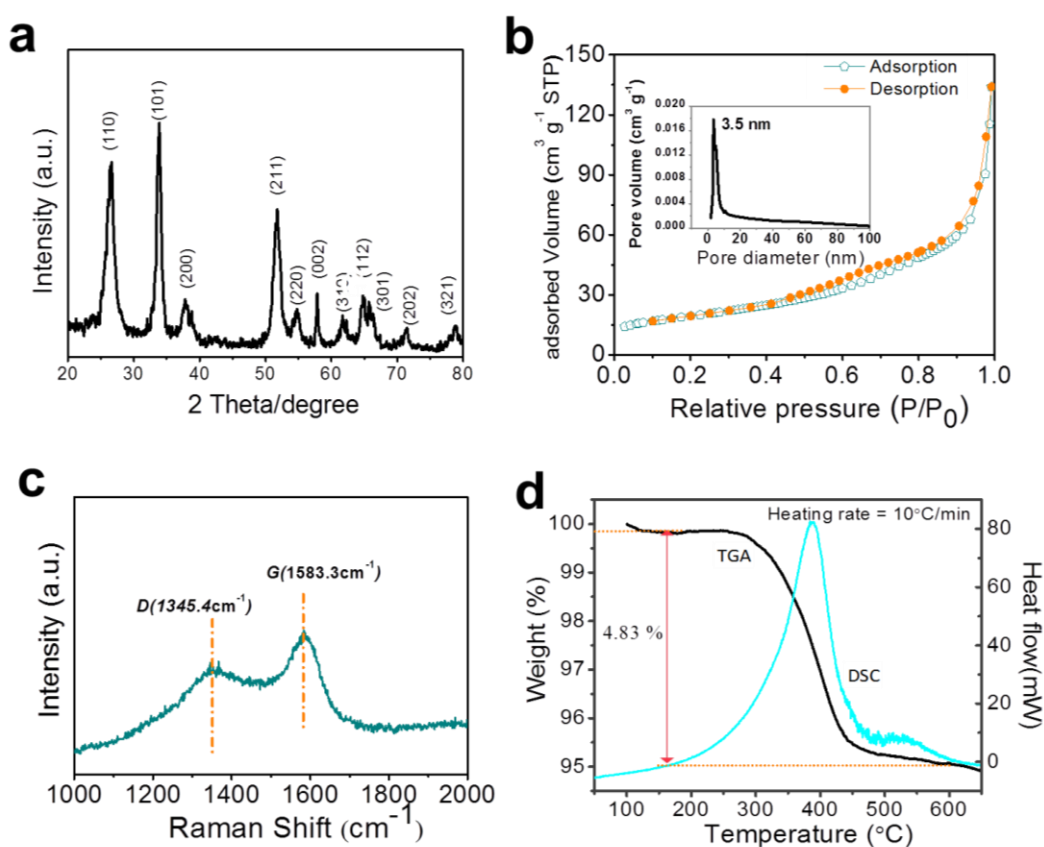
1
2 Figure S1. SEM image of SiO₂ nanospheres employed as removable templates for the preparation of
3 DSHSs and TSHSs
4



5
6 Figure S2. Element maps (a), EDS pattern (b), STEM image (c) and line scanning profiles of Sn, O
7 and C recorded along the line (d) of selected individual SnO₂ TSHSs.
8



1
2 Figure S3. XRD pattern (a), BET analysis (b), Raman spectrum (c) and TGA-DSC analysis (d) of the
3 SnO₂ DSHSs. The inset in (b) is pore size distribution curve of the SnO₂ DSHSs.
4

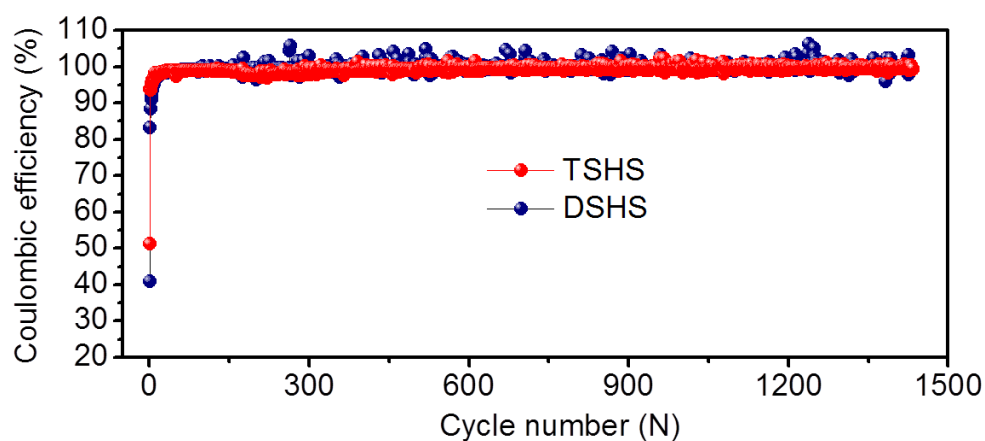


5
6 Figure S4. XRD pattern (a), BET analysis (b), Raman spectrum (c) and TGA-DSC analysis (d) of the
7 SnO₂ TSHSs. The inset in (b) is pore size distribution curve of the SnO₂ TSHSs.
8

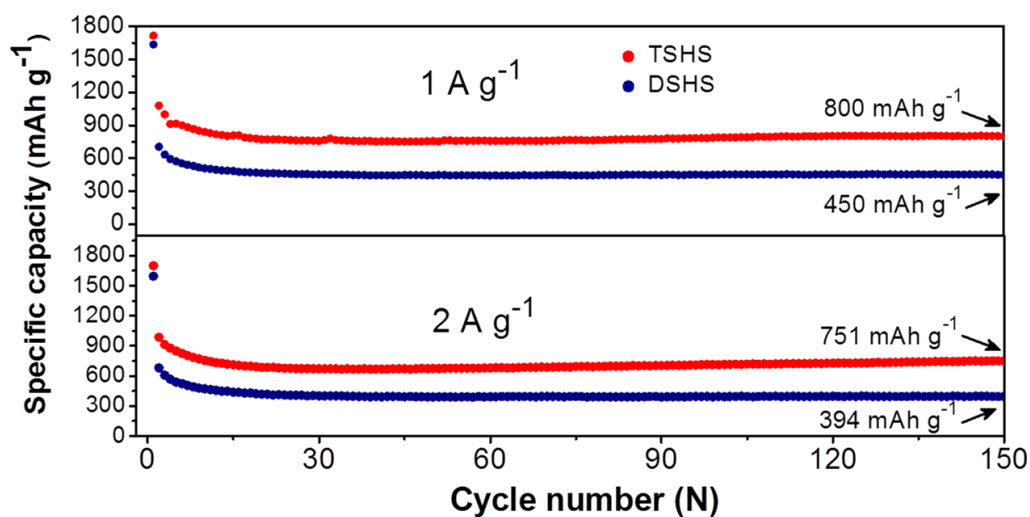
1 **Table S1.** Comprehensive performance comparison (specific capacity vs cycle vs current density) between SnO₂
 2 TSHS-based LIB and other SnO₂ anode-based LIBs.

Anode Materials	Cycle Number	Current Density (mA g ⁻¹)	Capacity (mAh g ⁻¹)	Voltage Range (V) vs. Li ⁺ /Li	Carbon Content(%)	References
Ultrasmall SnO ₂ Particles/ Carbon	2000	1400	443	0.01-1.5	60	[41]
SnO ₂ @TiO ₂ wire-in-tube	1000	400	393.3	0.005-1.5	/	[43]
Porous SnO ₂ submicrocubes	200	1000	516	0.01-2.0	29	[44]
GNRs/SnO ₂	50	100	825	0.01-2.5	19.5	[33]
TSHS	1450	500	1099	0.005-2.5	4.8	This work
	1200	4000	416			
SnO ₂ QDs@GO	2000	2000	477	0.01-3.0	12.3	[46]
graphene/SnO ₂ nanorod/carbon	350	1000	~750	0.01-3.0	31.88	[26]
Hybrid Cellular Nanosheets	300	200	914	0.01-3.0	59.4	[27]
SnO ₂ @N-CNF	300	1000	754	0.01-3.0	70.4	[45]
G@SnO ₂ @C	100	200	800	0.01-3.0	20	[40]
SnO ₂ /C nanohybrid	2000	2000	400	0.05-3.0	26	[39]
F-G/SnO ₂ @C	200	500	785	0.05-3.0	24.2	[42]

3
 4 *Results summarized from Figure 2e in the manuscript
 5
 6
 7



8
 9 Figure S5. Coulombic efficiency for the SnO₂ TSHS and DSHS electrodes during the long-term
 10 cycling process at a current density of 0.5 A g⁻¹.
 11
 12



1
2 Figure S6. Cycling performance of the SnO₂ TSHS and DSHS electrodes at different current densities
3 of 1 and 2 A g⁻¹.
4

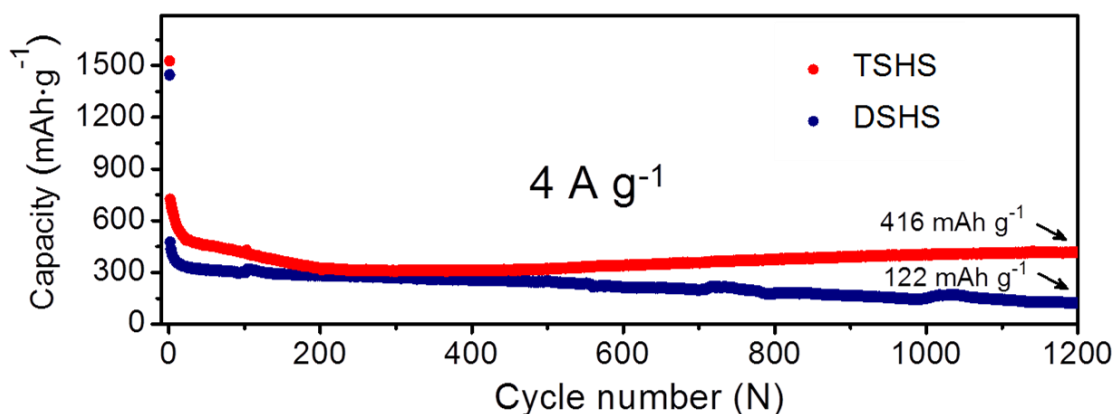
5 Table S2. Rate performance comparison between TSHS and DSHS.

Current density (A g ⁻¹)	Capacity (mAh g ⁻¹)		Capacity ratio (%)
	TSHS	DSHS	DSHS/TSHS
0.2	931	652	74.3
0.5	804	753	71.3
1	735	473	64.4
2	653	365	55.9
4	604	253	41.9
6	519	183	35.3
8	421	125	29.7
10	318	83	26.1
12	220	57	25.9
14	156	43	27.6
16	120	27	22.5
0.2	872	639	73.3

6

7

8



1
2 Figure S7. Cycling performance of the SnO₂ TSHS and DSHS electrodes at the current density of 4 A
3 g⁻¹.

4

5 S1 Reaction reversibility

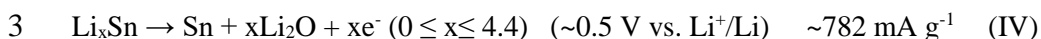
6 It is interesting that the high capacities, which even exceed the theoretical capacity (782 mAh g⁻¹:
7 SnO₂ → Sn + 2Li₂O; Sn + 4.4Li⁺ ↔ Li_{4.4}Sn) of SnO₂ materials, can be delivered by the SnO₂ TSHS
8 electrode, for example, 1099 mAh g⁻¹ at 0.5 A g⁻¹ and 800 mAh g⁻¹ at 1 A g⁻¹. To probe the
9 electrochemical reaction mechanism for high capacity uptake, CV measurements were carried out to
10 determine the lithiation/delithiation reactions involved over the SnO₂ electrodes (Figure S8).
11 Commercial SnO₂ nanoparticles (20–50 nm in size) coated with few-layer graphenized carbon (Figure
12 S9) were also selected for CV measurements together with the TSHSs and DSHSs. In theory, the full
13 lithiation/delithiation reactions for SnO₂ anode materials include three pairs of reversible redox
14 reactions, which involve the in-step reduction of SnO₂ to Li_xSn (reactions I-III) and the reversible
15 oxidation of Li_xSn to SnO₂ (reactions IV-VI), giving a high theoretical capacity of 1494 mAh g⁻¹.
16 However, the redox reactions between SnO₂ and Sn (reaction I and II, and V and VI) are almost
17 irreversible due to the poor reaction reversibility between Li₂O and Li⁺ ions^{3,4,5}, resulting in a lower
18 theoretical capacity of 782 mAh g⁻¹. Therefore, the reversible capacity of SnO₂ anodes highly depends
19 on the reversibility of the lithiation/delithiation reactions.

20 Reduction reactions/lithiation reactions:

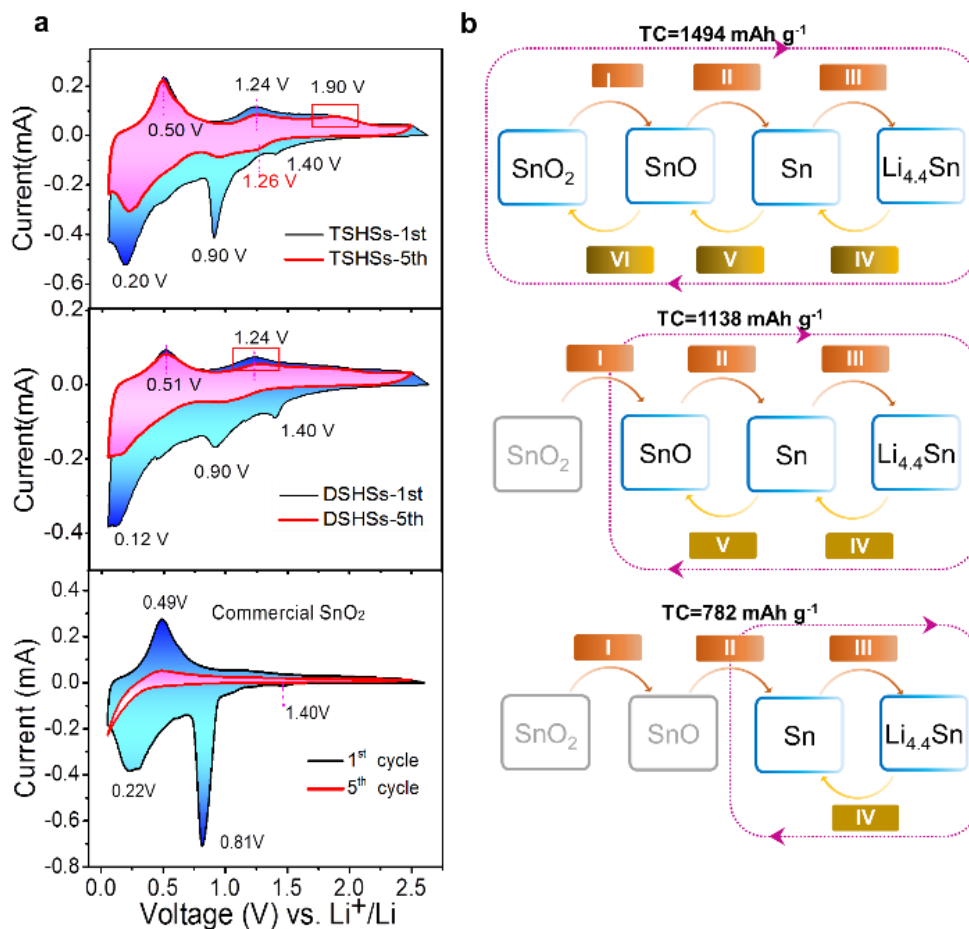




2 Oxidation reactions/delithiation reactions:



6



7

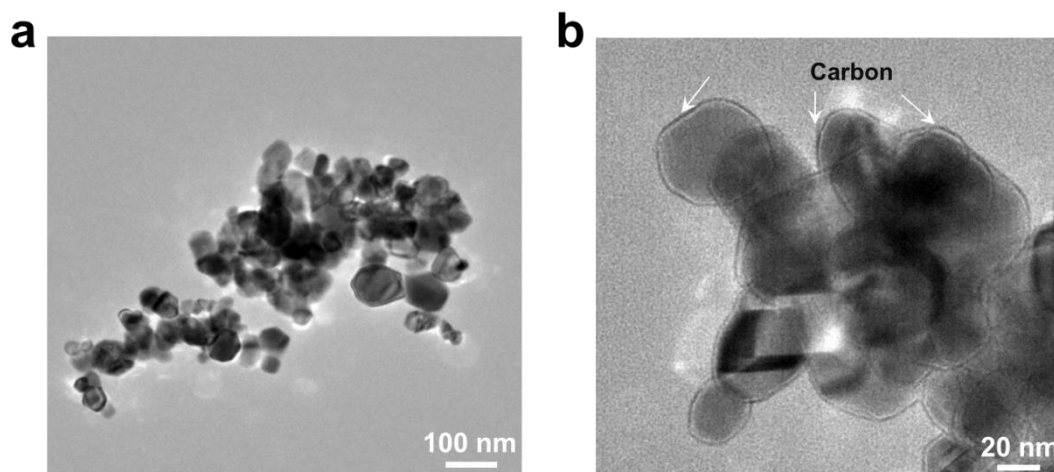
8 Figure S8. (a) Cyclic voltammetry curves of the SnO₂ TSHS and DSHS electrodes, and commercial
 9 SnO₂ electrode at 1st and 5th cycle at a scanning rate of 0.1 mV s⁻¹. (b) Schematic illustration shows
 10 different extent and theoretical capacity (TC) of reversible lithiation/delithiation reactions over the
 11 SnO₂ TSHS and DSHS electrodes, and commercial SnO₂ electrode after the first 5 cycles.

12 Figure S8a shows the CV curves of the three SnO₂ electrodes. In the first cathodic scan, all the
 13 electrodes display three peaks (~1.4, 0.9 and 0.2 V) corresponding to the reduction reactions of SnO₂
 14 and SnO and the alloying reaction of Sn, respectively, according to reactions I, II and III. However, in
 15 the reverse scan, only the SnO₂ TSHS electrode show three anodic peaks (~0.5, 1.24, and 1.90 V)
 16 corresponding to the reversible dealloying of Li_xSn and the oxidation of Sn and SnO, respectively, in

1 terms of reactions IV-VI. The peak (~ 1.90 V) for the DSHS electrode and the peaks (~ 1.24 and ~ 1.90
2 V) for the commercial SnO_2 electrode are almost absent, indicating the irreversible oxidations of SnO
3 (reaction VI) and Sn (reaction V) for the DSHS and commercial SnO_2 electrodes, respectively. The
4 difference in reaction reversibility for the three electrodes is further confirmed by the corresponding
5 CV curves in the fifth cycle. For example, the three pairs of redox reactions (I \leftrightarrow VI) are completely
6 reversible over the TSHS electrode, accompanied by a slight peak shift from ~ 1.4 to 1.26 V. However,
7 only two pairs of redox reactions (II \leftrightarrow V) and one pair of reactions (III \leftrightarrow IV) are reversible over the
8 DSHS electrode and commercial SnO_2 electrode, respectively.

9 Figure S8b illustrates the reversible redox reactions involved for the three electrodes, highlighting
10 the differences in their reaction reversibility and theoretical capacity. Accordingly, the high capacity of
11 the TSHS anode may be attributed to its high reaction reversibility, enabling a higher theoretical
12 capacity and reaction extent. The reaction reversibility also has a significant influence on cycling
13 performance and rate capability in addition to the battery capacity. As shown in Figure S10, the
14 commercial SnO_2 electrode with poor reaction reversibility shows poor performance in both cycling
15 stability and rate capability.

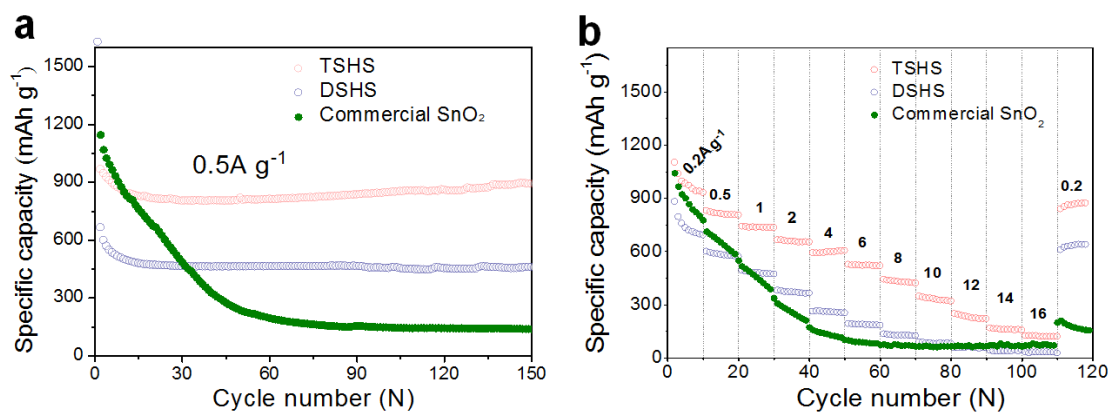
16



17

18 Figure S9. Low- (a) and high-resolution (b) TEM images of commercial SnO_2 nanoparticles coated
19 with carbon.

20



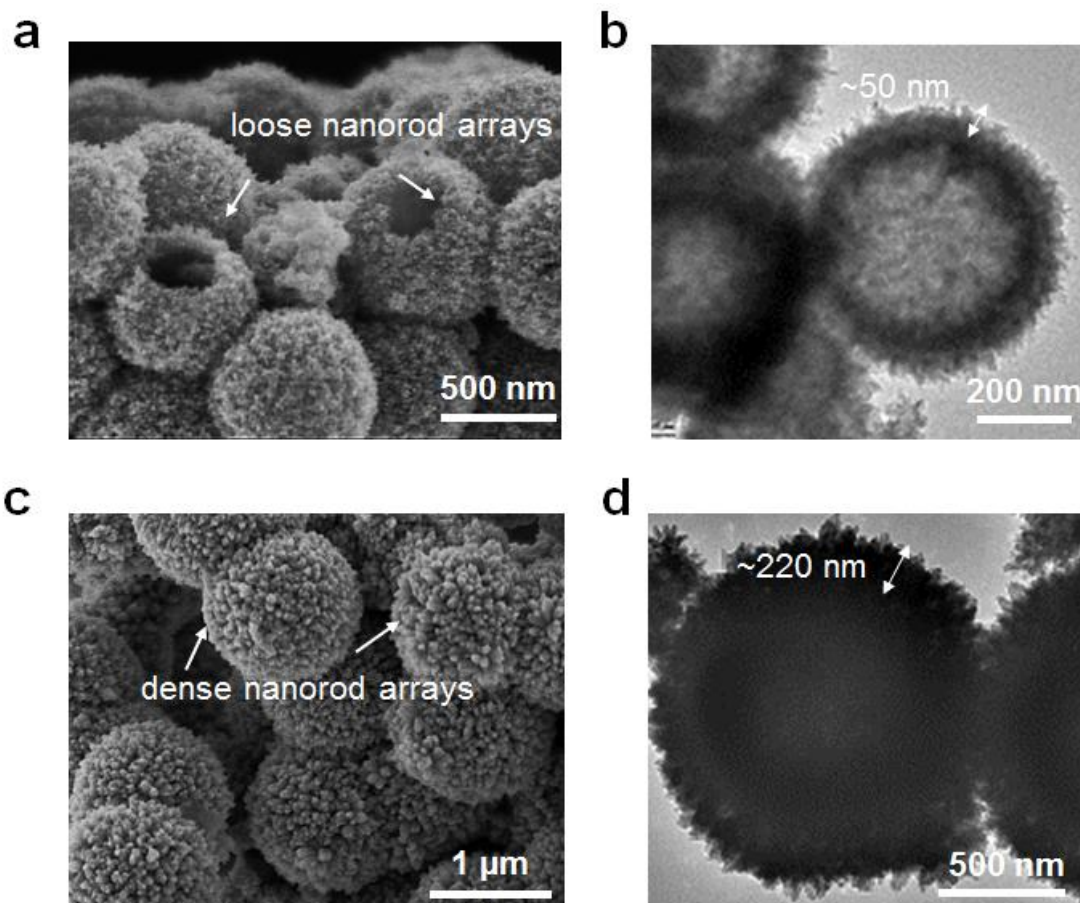
1
2 Figure S10. **a**, Cycling performance comparison of the SnO₂ TSHS, SnO₂ DSHS and commercial
3 SnO₂ electrodes tested at a current density of 0.5 A g⁻¹. **b**, Rate capability comparison of the SnO₂
4 TSHS, SnO₂ DSHS and commercial SnO₂ electrodes at current densities between 0.2 and 16 A g⁻¹,
5 respectively.

6
7 **S2. The effect of size and structural stability on the reaction reversibility and battery**
8 **performance.**

9 SnO₂ TSHSs with nanorods of different sizes and array densities in their outer shells were fabricated
10 and studied. Figure S11 shows the SEM images of two TSHS samples obtained with shorter (5 h) and
11 longer (30 h) nanorod growth times (denoted as TSHS-5h, TSHS-30h), compared with the typical
12 TSHSs (15 h). It can be seen that the TSHS-5h shows a thin outer shell of ~50 nm, consisting of
13 loosely arrayed short nanorods, which is much thinner than that of the typical TSHSs (110 nm) as well
14 as the TSHS-30h (~220 nm) made of densely arrayed long nanorods. Clearly, the size of nanorods in
15 the TSHS-5h is much smaller than that in the TSHS-30h, which may be reflected in their reaction
16 reversibility. As shown in Figure S12, the CV curves reveal that the three pairs of redox reactions
17 (I↔VI) are reversible for the TSHS-5h electrode, whereas only one pair (III↔IV) is reversible for the
18 TSHS-30h electrode, confirming the higher reaction reversibility of the TSHS-5h relative to the
19 TSHS-30h. However, both the TSHS-5h and TSHS-30h samples exhibit poor cycling performance and
20 inferior rate capability (Figure S13) compared with the typical TSHSs. For example, although high
21 capacities comparable to the typical TSHS electrode can be delivered by the two electrodes in the first
22 cycle, the continuous capacity decay for both electrodes, particularly the drastic capacity drop over the
23 first 10 cycles, results in poor cycling performance (Figure S13a). A phenomenon similar to the
24 serious capacity decay of the two electrodes was also observed in their rate performances, as shown in

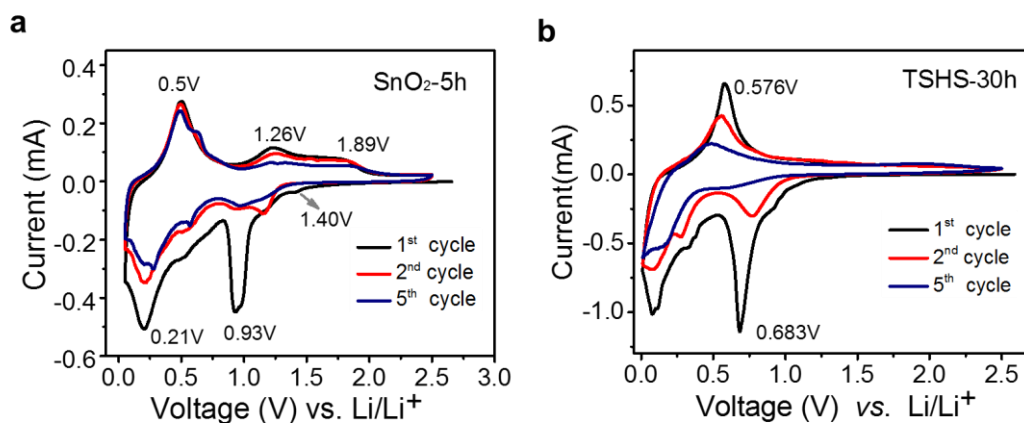
1 Figure S13b. The performance deterioration for the two samples may result from the structural
2 instability, that is, the collapse of the loose outer shells of the TSHS-5h and the falling off of
3 overgrown nanorods of the TSHS-30h. The results above demonstrate that, in addition to the size
4 effect, structural stability is also a crucial factor for high reaction reversibility and high battery
5 performance.

6



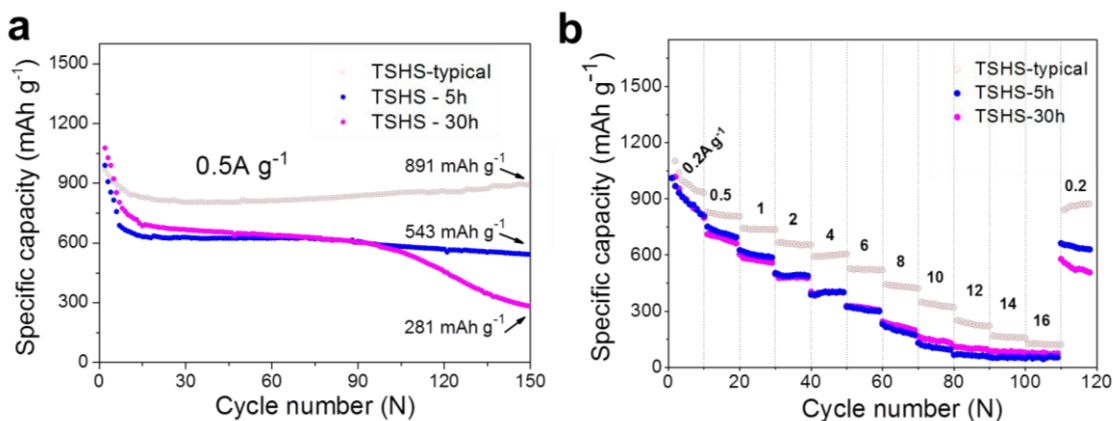
7

8 Figure S11. **a,b**, SEM (**a**) and TEM (**b**) images of SnO₂ TSHSs with a shorter growth time of 5h for
9 the third nanorod shell (TSHS-5h). **c, d**, SEM (**c**) and TEM (**d**) images of SnO₂ TSHSs with a longer
10 growth time of 30h for the third nanorod shell (TSHS-30h).



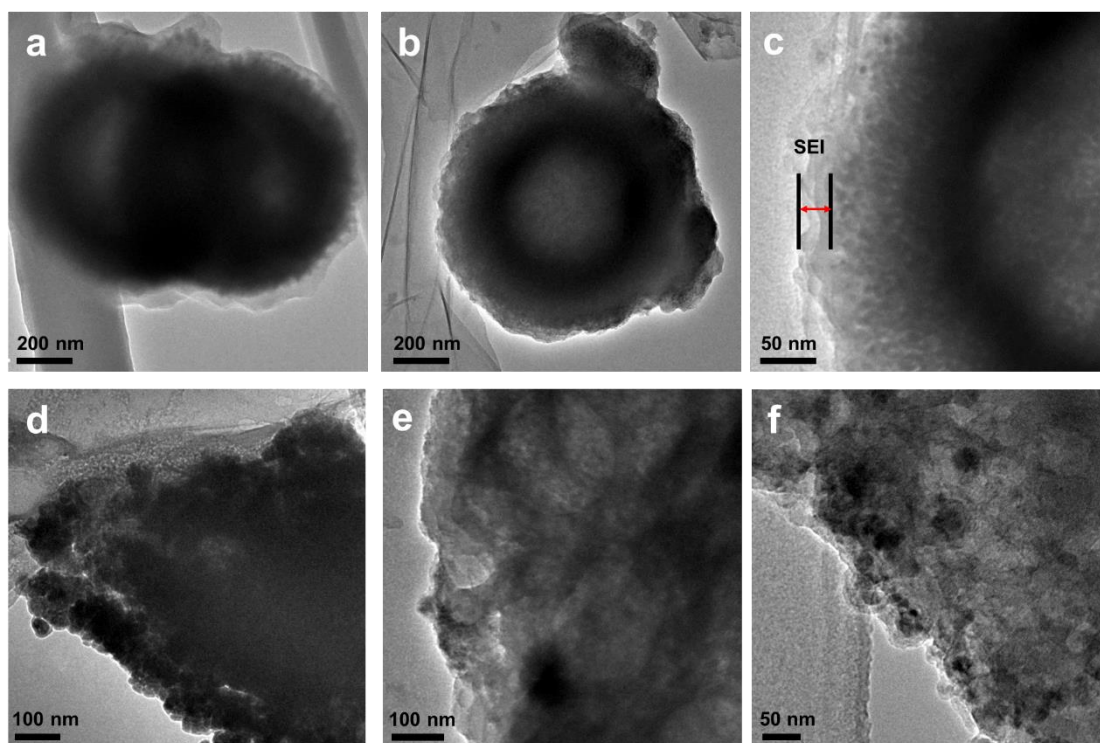
1
2

3 Figure S12. Cyclic voltammetry (CV) curves of the two electrodes based on TS_{HS}-5h (a) and TS_{HS}-
4 30h (b) at 1st, 2nd and 5th cycle at a scanning rate of 0.1 mV s⁻¹.

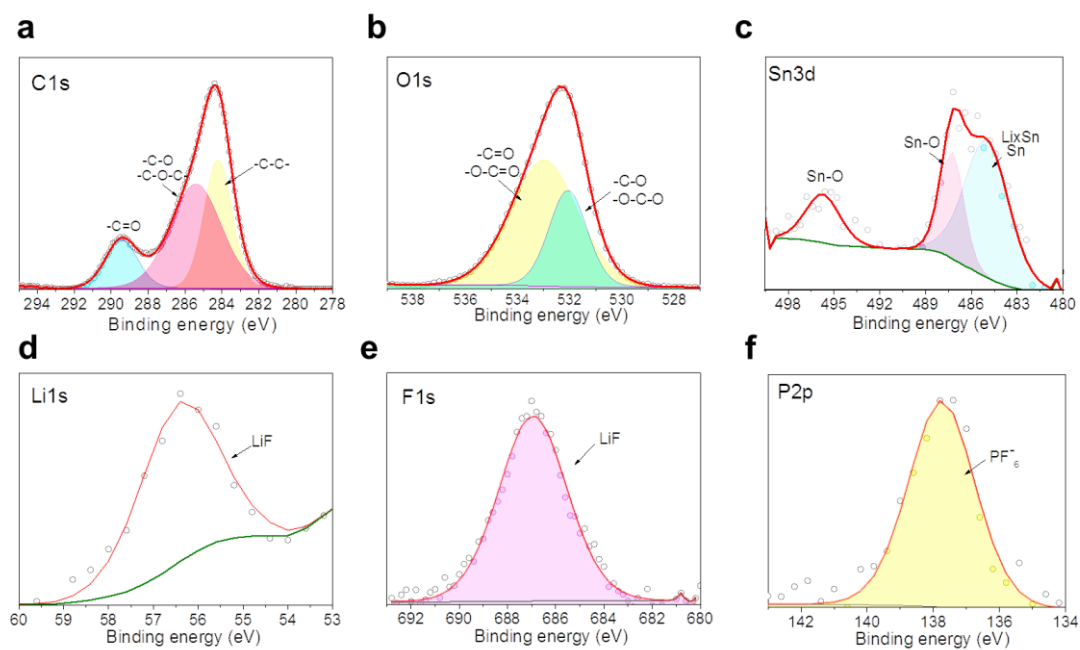


5
6
7
8
9

6 Figure S13. **a**, Cycling performance comparison of the typical SnO₂ TS_{HS} (15h), TS_{HS}-5h and
7 TS_{HS}-30h electrodes tested at a current density of 0.5 A g⁻¹. **b**, Rate capability comparison of the
8 typical SnO₂ TS_{HS}, TS_{HS}-5h and TS_{HS}-30h electrodes at current densities between 0.2 and 16 A g⁻¹.



1
2
3
4
5
6
Figure S14. TEM images of the solid electrolyte interphase film formed on TSHSs (a-c) and DSHSs (d-f) after cycling in electrolytes.



7
8
9
10
11
Figure S15. XPS spectra of compositions of the SEI film formed on TSHSs after cycling in electrolytes (a) carbon, (b) oxygen, (c) tin, (d) lithium, (e) fluoride, and (f) phosphorus, respectively.

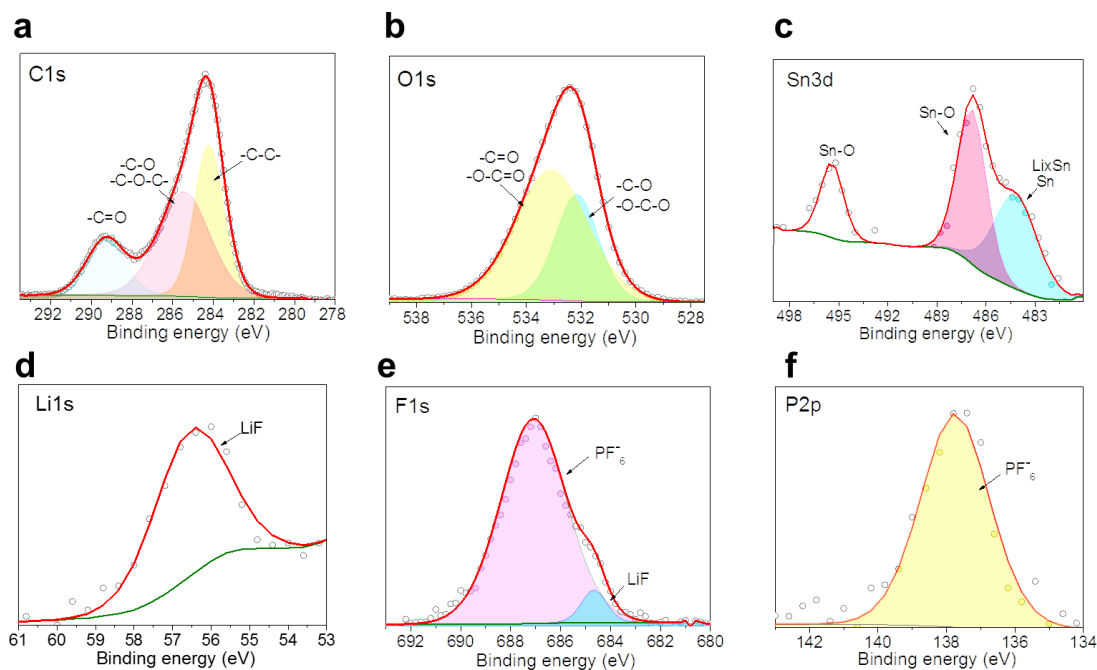
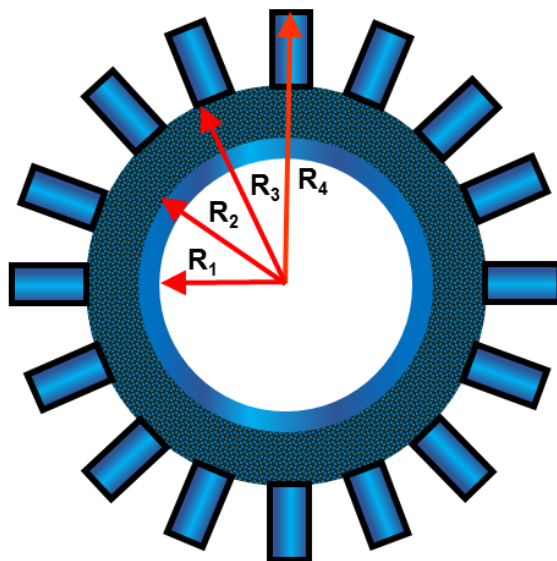


Figure S16. XPS spectra of compositions of the SEI film formed on DSHSs after cycling in electrolytes (a) carbon, (b) oxygen, (c) tin, (d) lithium, (e) fluoride, and (f) phosphorus, respectively.

Fig. S15 and Fig. S16 show the XPS spectra of the SEI formed on the active materials (TSHSs and DSHSs). A strong C1s peak at 284.4 eV is assigned to C-C bonds. The shoulder appearing in the vicinity of 285.5 eV is more likely to be from C-O and/ or C-O-C bonds, and the carbonate peak of these compounds is at 289.8 eV. The broad peak detected in the O1s spectrum at 532.5 eV corresponds to C-O and C=O bonds in the carbonyl configuration or lithium carbonate structure. A Li1s peak at 56.5 eV corresponds to compound of LiF. A shoulder F1s peak at about 684.8 eV is assigned to LiF. A broad peak at about 687.2 eV and P2p peak at 138 eV are attributed to the P-F bond.

S3. Calculations of volume changes of TSHSs and DSHSs according to *in situ* TEM characterization

It is well known that anode materials often undergo huge volume expansion upon lithiation. A larger volume expansion means a higher extent of lithium storage and is expressed as a higher capacity. Therefore, certain key factors such as volume change, volume expansion ratio, and expanded volume ratio are crucial for assessing the capacity or capacity contribution ratio for individual shells of the TSHSs/DSHSs. These important factors can be calculated in a relatively quantitative manner, according to *in situ* TEM characterization. Before calculation, R_1 , R_2 , R_3 and R_4 are defined as the inner/outer radii for the three shells, as shown in the figure below:



1

2

3 R_1 : inner radius of the first shell4 R_2 : outer radius of the first shell, or the inner radius of the second shell5 R_3 : outer radius of the second shell, or the inner radius of the third shell6 R_4 : outer radius of the third shell

7 According to these definitions, the volume of the three shells can be calculated as follows:

8 Volume of the first shell, $V_{1st} = 4/3\pi*(R_2^3 - R_1^3)$ (1)

9 Volume of the second shell, $V_{2nd} = 4/3\pi*(R_3^3 - R_2^3)$ (2);

10 Volume of the third shell, $V_{3rd} = 4/3\pi*(R_4^3 - R_3^3)$ (3);

11 Considering that the second shell consists of loosely aggregated $\text{SnO}_2@\text{C}$ nanodots with notable void
 12 space, the calculation for the second shell is carried out according to a modified equation 2', assuming
 13 the volume occupancy for SnO_2 nanodots in the shell is ~33%. Therefore, the equation for the
 14 equivalent volume of SnO_2 in the second shell is given as follows:

15
$$V_{2nd \text{ SnO}_2} = 4/3\pi*(R_3^3 - R_2^3) * 33\% \quad (2')$$

16 According to equations 1, 2' and 3, the volume expansion ratios for individual shells and the general
 17 volume expansion ratios for the DSHSs/TSHSs after lithiation can be calculated as follows:

18 volume expansion ratio for individual shells, $r_{v/v}^i = V_{lithiated}^i / V_{initial}^i$ ($i = 1^{st}, 2^{nd}, 3^{rd}$)19 general volume expansion ratio, $R_{v/v} = V_{lithiated}^{total} / V_{initial}^{total} = (V_{lithiated}^{1st} + V_{lithiated}^{2nd} +$
20 $V_{lithiated}^{3rd}) / (V_{initial}^{1st} + V_{initial}^{2nd} + V_{initial}^{3rd})$

1 The volume expansion ratio and general volume expansion ratio can reflect the extent of lithiation for
 2 individual shells and the TSHSs/DSHSs, respectively, which are also related to the capacity that can be
 3 delivered.

4 The expanded volume and the expanded volume ratio for each shell can also be calculated, and they
 5 are used to estimate the capacity contribution ratio of each shell to the total.

6 Expanded volume, $\Delta V^i = V^i_{\text{lithiated}} - V^i_{\text{initial}}$ (i = 1st, 2nd, 3rd)

7 Expanded volume ratio, that is, capacity contribution ratio,

8 $R^i_{\Delta V/\Delta V} = \Delta V^i/\Delta V_{\text{total}} = \Delta V^i/(\Delta V_{1\text{st}} + \Delta V_{2\text{nd}} + \Delta V_{3\text{rd}})$ (i = 1st, 2nd, 3rd shell)

9 The above equations are applicable for the TSHSs. For the DSHS calculations, only the parameters for
 10 the first and second shells are involved.

11 Accordingly, the calculations can be conducted based on the above definitions and analyses, which are
 12 listed in Table S3 below.

13

14 Table S3. Calculation results for key parameters related to the volume change after lithiation for the
 15 DSHS and TSHS.

	DSHS						TSHS						
	R_1 (nm)	R_2 (nm)	R_3 (nm)	R_1 (nm)	R_2 (nm)	R_3 (nm)	R_4 (nm)						
Initial	180	197	254	180	197	254	360						
Lithiated	208	228	311	218	235	310	468						
	V_{Initial} (nm ³)	$V_{\text{lithiated}}$ (nm ³)	r'_{VV}	R_{VV}	ΔV	$R'_{\Delta V/\Delta V}$	V_{Initial} (nm ³)	$V_{\text{lithiated}}$ (nm ³)	r'_{VV}	R_{VV}	ΔV	$R'_{\Delta V/\Delta V}$	
1st shell	7.58E6	1.19E7	157.4%		4.32E6	24.9%	7.58E6	1.10E7	145.1%		3.42E6	1.78%	
2nd shell	3.67E7	7.62E7	208.6%	188.1%	3.95E7	75.1%	3.74E7	7.03E7	187.9%		3.29E7	5.65%	
	*33%	*33%			*33%		*33%	*33%			231.8%	*33%	
3rd shell	x	x	x	x	x	x	1.26E8	3.04E8	242%		1.78E8	92.57%	

16

17 In addition, to ensure the validity of the conclusions, calculations assuming two ultimate values (0%
 18 and 100%) of volume occupancy for SnO₂ nanodots in the second layers have also been performed.

19 The results are listed in the tables below (Tab A and B), which also give the same conclusion as that
 20 obtained by the calculation adopting the volume occupancy of 33%.

21

22

1 Tab A. Calculation results for key parameters related to the volume change after lithiation for the
 2 DSHS and TSHS (assuming the volume occupancy for SnO₂ nanodots in the second shell is **0%**)

	DSHS						TSHS						
	R_1 (nm)	R_2 (nm)	R_3 (nm)				R_1 (nm)	R_2 (nm)	R_3 (nm)	R_4 (nm)			
Initial	180	197	254				180	197	254	360			
Lithiated	208	228	311				218	235	310	468			
	$V_{initial}$ (nm ³)	$V_{lithiated}$ (nm ³)	r'_{VV}	R_{VV}	$\Delta V'$	$R'_{\Delta V/\Delta V}$	$V_{initial}$ (nm ³)	$V_{lithiated}$ (nm ³)	r'_{VV}	R_{VV}	$\Delta V'$	$R'_{\Delta V/\Delta V}$	
1st shell	7.58E6	1.19E7	157.4%		4.32E6	100%	7.58E6	1.10E7	145.1%		3.42E6	1.89%	
2nd shell	0	0	×	157.4	0	0	0	0	×		0	0	235.8%
3rd shell	×	×	×	×	×	×	1.26E8	3.04E8	242%		1.78E8	98.1%	

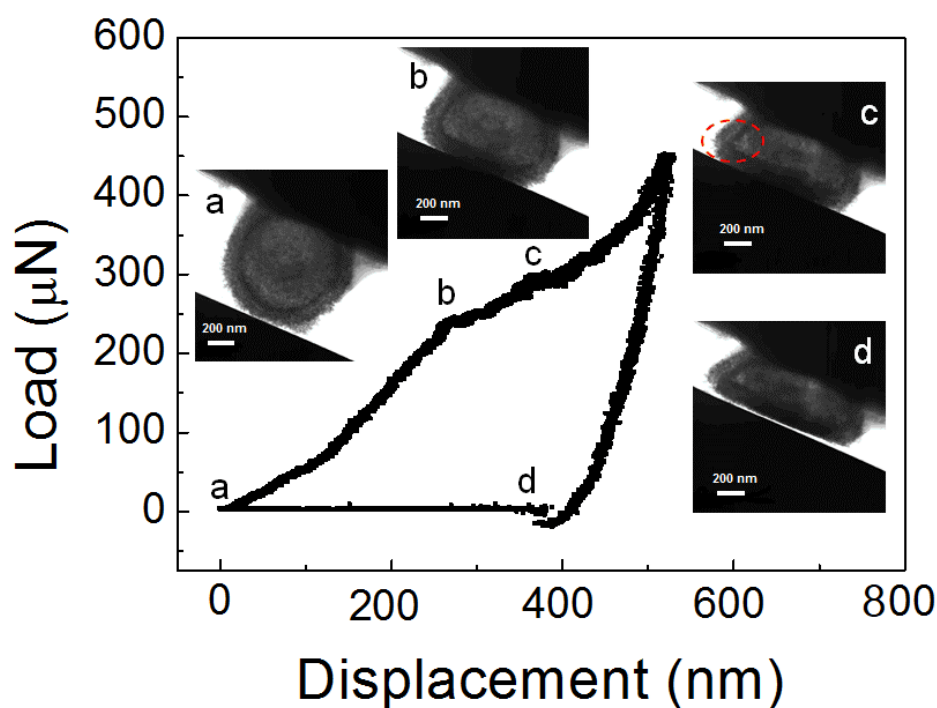
4 Tab B. Calculation results for key parameters related to the volume change after lithiation for the
 5 DSHS and TSHS (assuming the volume occupancy for SnO₂ nanodots in the second shell is **100%**)

	DSHS						TSHS						
	R_1 (nm)	R_2 (nm)	R_3 (nm)				R_1 (nm)	R_2 (nm)	R_3 (nm)	R_4 (nm)			
Initial	180	197	254				180	197	254	360			
Lithiated	208	228	311				218	235	310	468			
	$V_{initial}$ (nm ³)	$V_{lithiated}$ (nm ³)	r'_{VV}	R_{VV}	$\Delta V'$	$R'_{\Delta V/\Delta V}$	$V_{initial}$ (nm ³)	$V_{lithiated}$ (nm ³)	r'_{VV}	R_{VV}	$\Delta V'$	$R'_{\Delta V/\Delta V}$	
1st shell	7.58E6	1.19E7	157.4%		4.32E6	9.86%	7.58E6	1.10E7	145.1%	7.58E6		3.42E6	1.60%
2nd shell	3.67E7	7.62E7	208.6%	199.0%	3.95E7	90.14%	3.74E7	7.03E7	187.9%	3.67E7		3.29E7	15.35
												225.3%	
3rd shell	×	×	×	×	×	×	1.26E8	3.04E8	242%	×		1.78E8	83.05%

7 **S4. Mechanics analysis**

8 The load-displacement curve of a typical compression test on an individual TSHS is demonstrated
 9 in Fig. S17. Selected frames (inset a-d in Fig. S17) extracted from the video exhibited four different
 10 loading regimes marked as a-d in Fig. S17, respectively. In inset a, the tungsten punch just contacts the
 11 TSHS while no force is detected. From a to b, the loading force increases monotonically with
 12 continuous and smooth slope, suggesting that the TSHS deforms elastically. Then, a nano-sized crack
 13 conceives and propagates, resulting in a dramatic lowering of the slope in the loading-displacement
 14 curve. The crack is visible and marked by a red dashed ellipse in inset c. Interestingly, even with the
 15 formation of the crack, the loading force keeps increasing, and the TSHS does not fracture and/or

1 break into pieces as commonly observed in other cases¹. Finally, the TSHS is compressed into a pie-
 2 like shape as displayed in inset d.



3
 4 Figure S17. Load-displacement curve of a single particle under displacement control mode.

5 **Mechanics simulations**

6 To better understand the structural stability of the DSHSs and TSHSs during the lithiation process,
 7 we adopted an elastic-plastic model coupled to Li diffusion to evaluate the lithiation-induced
 8 deformation and stress states. The structure is connected to the reference electrode and subjected to a
 9 constant lithium flux (J_0) on the contact surface, where the Li-ion concentration (C) is constant.
 10 Diffusion is described by a nonlinear equation with diffusivities depending on the local Li
 11 concentration, thereby obtaining a two-phase lithiation region and a sharp phase boundary between
 12 lithiated and unlithiated materials. Our simulations aim at obtaining the mechanisms of stress to
 13 analyze the mechanics of deformation and fracture. Thus, we assume that the effective diffusion
 14 coefficient, D , is described by a simple non-linear function

$$15 \quad D = D_0 C (d^2 f / dC^2)$$

16 where D_0 is the diffusion constant and f is the free energy. f is based on a regulation solution model,
 17 which can be described as

$$18 \quad f = \varphi c(1-c) + [c \ln c + (1-c) \ln(1-c)]$$

1 where c is the normalized Li-ion concentration (C/C_0) and φ is a constant used to control the
 2 concentration profile near the reaction front. Thus, the effective diffusion coefficient D can be
 3 represented as

$$4 \quad D = D_0 [1 / (1 - c) - 2\varphi c]$$

5 The normalized Li-ion concentration of c is governed by the maximum Li-ion concentration (C_0) at the
 6 fully lithiated area. In diffusion simulations, c behind the reaction interface can quickly reach a high
 7 value of ~ 1 , whereas that ahead of the front remains nearly ~ 0 . This effect produces a sharp reaction
 8 front, which provides a basis for further analysis of stress.

9 We adopt an ideal elastic-plastic model to describe the lithiation-induced deformation. The
 10 increment of the total strain, $d\varepsilon_{ij}$ is taken to be the sum of three contributions, that is

$$11 \quad d\varepsilon_{ij} = d\varepsilon^c_{ij} + d\varepsilon^e_{ij} + d\varepsilon^p_{ij}$$

12 where $d\varepsilon^c_{ij}$, $d\varepsilon^e_{ij}$ and $d\varepsilon^p_{ij}$ are the lithiation-induced chemical strain, elastic strain, and plastic strain,
 13 respectively.

14 The increment of $d\varepsilon^e_{ij}$ is proportional to that of the Li-ion concentration

$$15 \quad d\varepsilon^e_{ij} = \beta_{ij} dc$$

16 with $\beta = \Omega \delta_{ij} / 3$ representing the expansion coefficient. Here, Ω is the partial molar volume of solute,
 17 $\delta_{ij} = 1$ for $i = j$ and otherwise, $\delta_{ij} = 0$.

18 The increment of the elastic strain, $d\varepsilon^e_{ij}$, obeys Hooke's law

$$19 \quad d\varepsilon^e_{ij} = 1/E [(1 + \nu)d\sigma_{ij} - \nu d\sigma_{kk} \delta_{ij}]$$

20 where E is Young's modulus and ν is Poisson's ratio; repeated indices mean summation.

21 The increment of plastic strain, $d\varepsilon^p_{ij}$, abides the classic J_2 -flow rule, namely, plastic yielding
 22 occurs when the von Mises effective stress, σ_{eq} equals the yield strength σ_Y .

$$23 \quad \sigma_{eq} = (3s_{ij}s_{ij}/2)^{1/2}$$

24 Here, s_{ij} is the deviatoric stress, $s_{ij} = \sigma_{ij} - \sigma_{kk}\delta_{ij}/3$

25 and $d\varepsilon^p_{ij}$ is proportional to s_{ij} , given by

$$26 \quad d\varepsilon^p_{ij} = d\lambda s_{ij}$$

27 where λ is a scalar coefficient that can be determined by solving the boundary value problem.

28 The Young's modulus of the SnO₂ is dependent on the Li concentration. However, considering
 29 the existence of porosity in the second layer, the Young's modulus of porous SnO₂ can be estimated
 30 by $Y = A(1 - P)^3$, where $A = 200$ GPa is a constant and P is the porosity. For $P = 0.33$, the Young's
 31

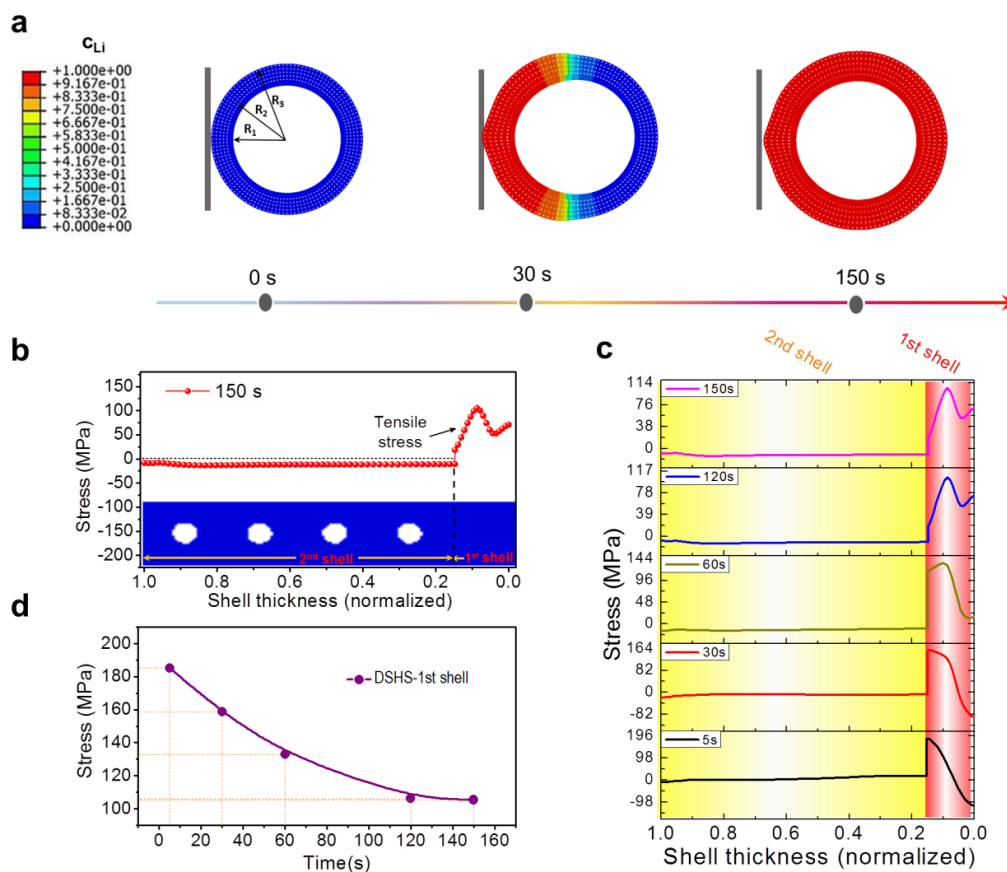
1 modulus of the first shell is approximately 59 GPa.

2 We numerically implemented the above diffusion and constitutive equations of elastic-plastic
3 deformation model by using the finite element package ABAQUS. The Li and stress-strain fields were
4 incrementally updated using an implicit coupled temperature-displacement procedure in
5 ABAQUS/Standard. To describe the evolution of diffusion and associated stress generation, fully
6 coupled thermal diffusion-stress analysis was performed in direct finite element simulations.

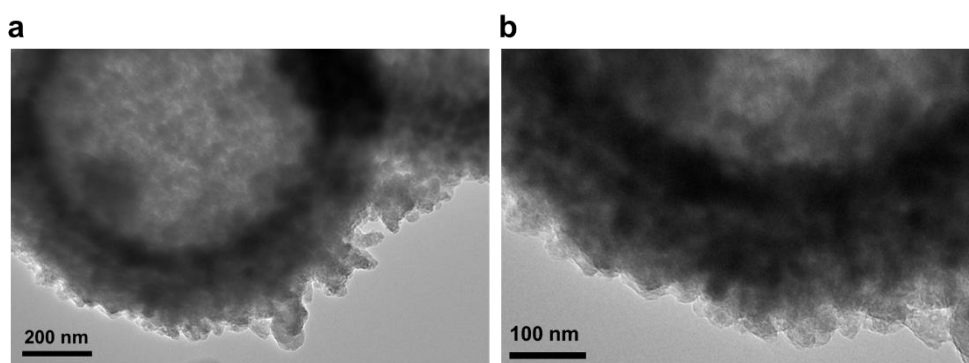
7 The electrode material is taken to be a homogeneous and isotropic elastic-perfectly plastic solid
8 undergoing plane strain quasi-static deformation. Transient analysis, where the diffusion equations are
9 integrated with a backward-difference scheme and the computed system is solved by Newton's
10 method, is carried out in ABAQUS/Standard. A uniform quadrilateral structured mesh is used. Fine
11 mesh is applied in the region of stress concentration, and the element size is set to equal 1% of the
12 global dimension with the axisymmetric condition. Here, the diffusion properties are assigned to
13 generate a stable two-phase structure. We take $\phi = 1.95$ and assign a constant C_0 on the surface. For
14 numerical stability, the maximum D is limited at $10^4 D_0$.

15

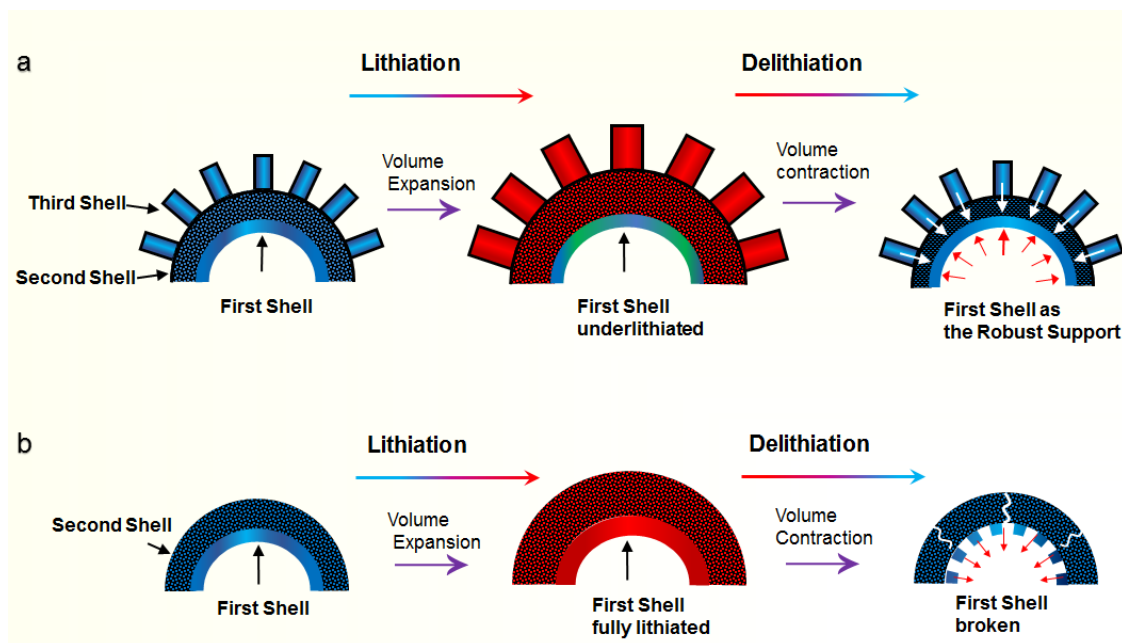
16



1
2 Figure S18. a, Maximum principal stress contours on deformed shapes of DSHS during lithiation from
3 0s to 150s. b, Evolution of stress in the first and second shells of a DSHS after lithiation. c, the
4 hoop stress evolution of first and second shell of the DSHS during lithiation. d, the peak value of tensile
5 stress in first shell as function of time.



6
7
8 Figure S19. TEM images of a TSHS after lithiation
9



1
2
3 Figure S20. Schematic illustration shows different shell-evolution behaviors upon
4 lithiation/delithiation in TSHS (a) and DSHS (b) leading to structure preservation (a) and collapse (b),
5 respectively.

6 7 **References for the Supporting Information**

- 8
9 [1] Z. W. Shan, G. Adesso, A. Cabot, M. P. Sherburne, S. A. Asif, O. L. Warren, D. C.
10 Chrzan, A. M. Minor, A. P. Alivisatos, *Nature materials* 2008, **7**, 947-952.
11 [2] A. Minor, J. Ye, C. Chisholm, R. Mishra, O. L. Warren, *Microscopy and*
12 *Microanalysis* 2009, **15**, 1184-1185.
13 [3] D. N. Wang, J. L. Yang, X. F. Li, D. S. Geng, R. Li, M. Cai, T. K. Sham, X. L. Sun,
14 *Energy Environ. Sci.* **2013**, **6**, 2900-2906.
15 [4] V. Aravindan, K. B. Jinesh, R. R. Prabhakar, V. S. Kale, S. Madhavi, *Nano Energy*
16 **2013**, **2**, 720-725.
17 [5] R. Hu, D. Chen, G. Waller, Y. Ouyang, Y. Chen, B. Zhao, B. Rainwater, C. Yang, M.
18 Zhu, M. Liu, *Energy Environ. Sci.* **2016**, **9**, 595-603.
19
20